nature communications

Article

https://doi.org/10.1038/s41467-024-54094-4

Non-linear elasticity, earthquake triggering and seasonal hydrological forcing along the Irpinia fault, Southern Italy

Received: 8 March 2024

Accepted: 1 November 2024

Published online: 13 November 2024

Check for updates

Stefania Tarantino [1] ✉, Piero Poli [2], Nicola D'Agostino [3], Maurizio Vassallo [1], Gaetano Festa [4], Gerardo Ventafridda [5] & Aldo Zollo [4]

Pump-probe experiments investigate the strain sensitivity of crustal elastic properties, showing nonlinear variations during the strain cycle. In the laboratory, pre-seismic reductions in seismic velocity indicate that asperity contacts within the fault zone begin to fail before the macroscopic frictional sliding. The recognition of such effects in natural seismic-cycles has been challenging. Here we exploit seasonal hydrological strains, performing a natural analogue to a quasi-static laboratory pump-probe experiment to investigate the nonlinear strain sensitivity of crustal rocks and its role in seismic failure along the tectonically-active Irpinia Fault System (Southern Italy). By comparing 14-years-long series of spring discharge, strain, seismic velocity variations and earthquakes rate, we find that seismicity peaks during maximum hydrological forcing and minimum seismic velocity. Seasonal strains of ~10^{-6} are required for both earthquake triggering and significant nonlinearity effects arising from modulus reduction. We suggest that, for faults in a critical state, cyclical softening may lead to failure and seasonal seismicity.

While linear elasticity is widely employed in Earth science applications[1], the heterogenous nature of geomaterials makes them to behave in a non-linear way, as it can be revealed by variations in elastic modulus[2], hysteresis[3], slow dynamics[4], when rocks are subjected to strain perturbations[5]. Pump-probe experiments are nowadays widely used to quantify the non-linear behavior of rocks in laboratory[2,5–7] and provide fundamental insights about the relationships between non-linear elastic parameters and physical properties of materials, such as damage[7,8] or presence and amount of fluids[9–11], among others[2,6,12–15]. All these variables have a key role in controlling the seismic cycle[16,17] and the physics of earthquakes nucleation[18,19]. It has been suggested that progressive loading produces distributed microcracks that at some stage begin to coalesce onto a volumetric region of concentrated damage that, when a critical level is exceeded, experiences instability that leads to rupture[17]. In laboratory[20] accelerated fault creep causes elastic moduli (and seismic velocity) reductions during the preparatory phase preceding failure, as asperity contacts begin to fail before macroscopic frictional sliding. This can be also related to rock damage. A temporary reduction in the fault core modulus could induce fault slip for a fault already near failure[18]. It is thus crucial to assess the non-linear response of crustal rocks by investigating behaviors associated with stress, pore pressure, permeability, material failure, and rock damage in the Earth in the same way as in laboratory[2,20–22]. The advent of ambient noise seismology[23] offers to scientists the possibility to develop ad-hoc pump-probe experiments, measuring in-situ the velocity changes ($\delta v/v$) from estimates of the Green's function[23] (the probe), excited by (the pump) natural (mainly tidal strains[12,24]) or man-made strain. These studies revealed significant non-linearity for shallow crustal rocks[13], enhanced in complex settings such as fault systems[8,25] and volcanic regions[9,13].

Following previous works on non-linearity[8,12,24], β represents the second order, quadratic, coefficient of the stress-strain elastic

[1]Istituto Nazionale di Geofisica e Vulcanologia, L'Aquila, Italy. [2]Department of Geoscience, University of Padova, Padova, Italy. [3]Istituto Nazionale Geofisica e Vulcanologia, Rome, Italy. [4]Department of Physics, University of Napoli, Napoli, Italy. [5]Approvvigionamento Idrico (DIRAP), Acquedotto Pugliese S.p.A, Bari, Italy. ✉e-mail: stefania.tarantino@ingv.it

relationship[5]:

$$\sigma = M\left[\varepsilon + \beta\varepsilon^2 + f(\varepsilon, \dot{\varepsilon})\right] \quad (1)$$

where σ is the stress, M is the elastic modulus, ε is the strain and f indicates the hysteretic components dependent on strain and strain rate. The strain sensitivity β[5,24] of seismogenic rocks can be estimated through a quantitative comparison of strain ε vs $\delta v/v$ curves[5,24]:

$$\frac{\delta v}{v} = \alpha + \beta\varepsilon \quad (2)$$

where α is an offset.

A value of β different from zero indicates non-linearity[13,26] and increases with the degree of the material damage and density of cracks[7]. Negative values of the strain sensitivity β have been interpreted in terms of decrease (increase) of seismic velocities under dilatational (contractional) strain operated by opening (closing)[27] of preexisting cracks in the crust[13].

In this study we perform a 14-years long-term analysis based on a natural analog of a pump-probe experiment to assess the non-linear behavior of the seismogenic volume in the Irpinia Fault Zone (IFZ, Fig. 1), which hosted the largest (Ms 6.9) instrumentally recorded earthquake in Italy[28]. Here we measured $\delta v/v$ induced by annual strain variations originating from recharging groundwater in karst aquifers[29,30], that significantly extends the temporal tidal forcing employed in previous works[14,24]. We show that hydrological processes induce nearly periodic, anisotropic fluctuations of horizontal strain[31,32] (which we used as a pump) associated with seasonal modulation of seismicity. We employ ambient seismic noise correlation[23] to track the temporal evolution of $\delta v/v$ in two sites (MCRV and CAFE, Fig. 1; see "Methods"), representative of the variable hydrological forcing

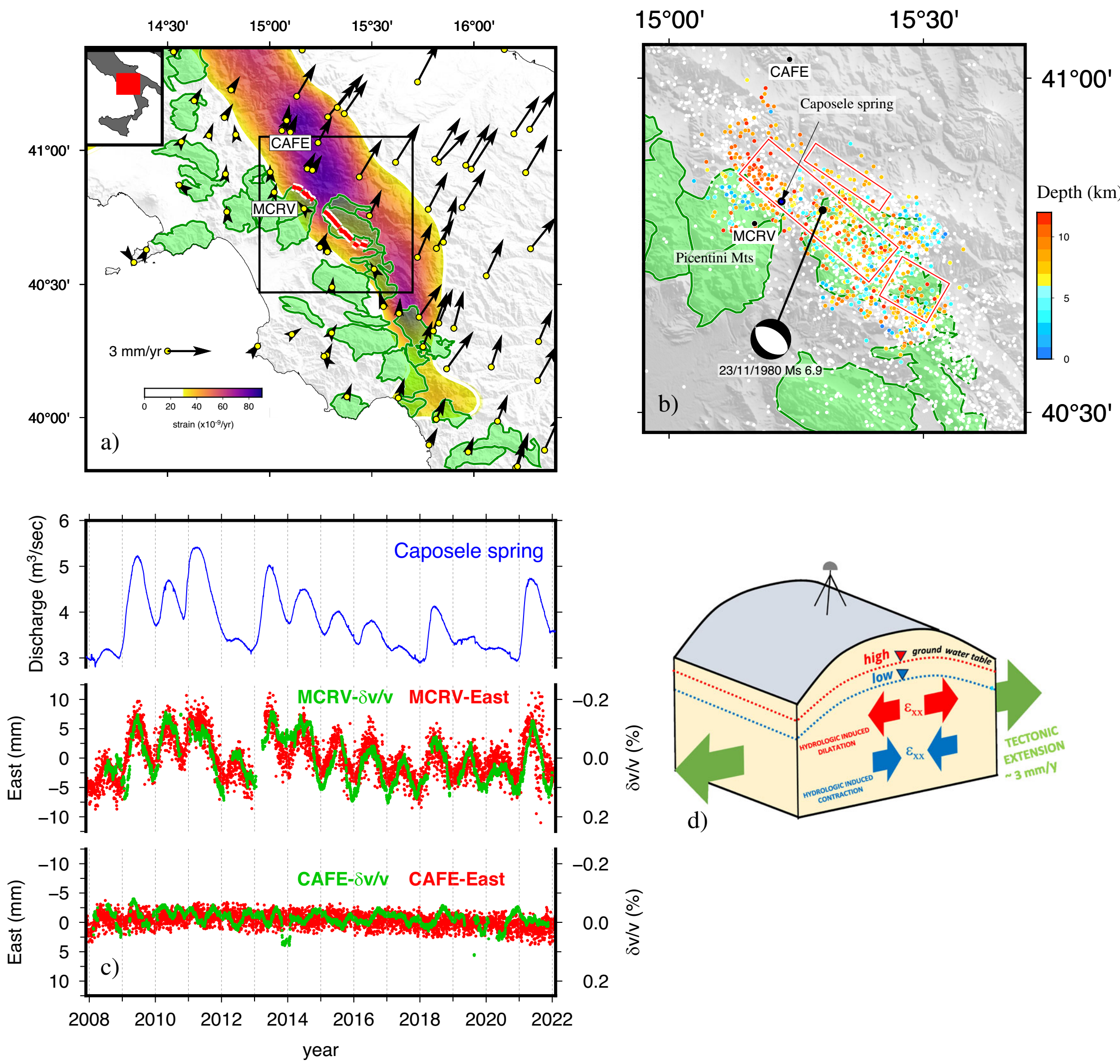

Fig. 1 | Summary of observations. a Map of the study area. Global Positioning System velocities in a Tyrrhenian reference frame[43]. The trace of Irpinia[70] is shown in red. Carbonate rocks are represented with green overlays. Background color-coding shows the secular tectonic strain rate (second invariant of the strain rate tensor). The inset shows the location of the study area in Italy. **b** Enlarged map (area enclosed by the black line in a) showing 2008–2022 seismicity from the Irpinia Seismic Network. Colored dots represent the considered declustered seismicity within the first 12 km of depth and above the completeness magnitude, white dots represent other not-considered seismic events. Global Centroid Moment Tensor focal solution and surface projections of the three faults[28] responsible for Ms 6.9, 1980 Irpinia earthquake with its focal mechanism; green patches enclose shallow carbonates rocks; **c** Time series of hydrological, seismological and geodetic observations. The upper panel shows the discharge measured at Caposele spring. Lower panels show velocity variations (green circles, inverted sign) for coda waves time lapse using empirical Green's functions reconstructed by autocorrelation of seismic noise recorded at MCRV and CAFE in the frequency band of 0.5- to 1-Hz (blue dots) together with East components of displacement at the same stations (red circles); **d** conceptual model of the modulation of crustal deformation induced by variable hydraulic head in karst aquifers. ε_{xx} indicates the horizontal strain in the ENE-WSW direction.

conditions, that we used as the probe to measure the non-linear elastic response of crustal rocks to strain fluctuations. Our analysis reveals a negative value for β in agreement with previous natural[12,13,24] and laboratory experiments[2,7,21], related to seasonal cycling of material damage along the IFZ and associated with seasonal modulation of seismicity. Our results highlight the dependence of seasonal seismicity on the non-linear rock behavior, which calls to improve our understanding of the role of elastic non-linearity and its effect on frictional properties in controlling the triggering of earthquakes along major seismogenic faults[8,33–40].

Results

Hydrological forcing and variations of seismic velocity and strain

The Caposele spring[29] provides a unique, 100-years-long, hydrological dataset of discharge (average ~4 m^3/s) from the karst aquifer of the Picentini Mountains (Fig. 1) hosted in extensively fractured, 2–3 km-thick, allochthonous, Mesozoic carbonates[41]. As no manmade modifications occur in its catchment, this spring is strictly controlled by climate trends[29] and is regionally-representative of the variations of hydrological forcing operated by the karst aquifers with maximum/minimum recharge in May-July and November-January, respectively[29,30]. To investigate the effects of hydrological forcing on crustal elastic properties, we calculated the velocity variations $\delta v/v$ from 14 years (January 2008-December 2021) of seismic data recorded at MCRV and CAFE stations (Fig. 1). Both sites (with co-located seismic and GPS receivers) are located within the tectonically deforming belt along the Apennines (Fig. 1a) but at variable distances from the IFZ and the karst aquifer. The recent microseismicity (local magnitude $-0.4 \leq M_L \leq 3.7$) occurring in the investigated region is characterized by normal fault mechanism[42], in agreement with the regional strain field[43] and the geometry and slip of the faults involved in the *Ms 6.9, 1980* Irpinia earthquake[28]. We used ambient noise correlations from single station measurements to apply the Coda Wave interferometry method[23] (CWI, see Methods) in a time-lapse of 10–50 s after zero time (ballistic waves arrival time). The time series of $\delta v/v$ (Fig. 1c) at MCRV reveal up to ~0.2% velocity variations which closely tracks the evolution of spring discharge and the GPS horizontal displacement (Fig. 1c). At MCRV we found that peaks of eastward displacement, which correspond to a transient, recoverable dilatational strain in the shallow crust across the karst aquifer[31,32], are correlated with negative peaks in the velocity of seismic waves, similarly to observations in other Apenninic regions[25,44]. The opposite occurs for negative Eastward displacements with contractional strains and significant increase of seismic velocities. At CAFE, located outside the karst aquifer region but inside the actively-deforming tectonic belt (Fig. 1a), we observe an order of magnitude smaller fractional seismic velocity change (~0.03%), and a GPS time series insensitive to seasonal variations, which document the absence of any relevant hydrological forcing. The seasonal velocity variations observed at MCRV are higher than those observed in other regions in the same tectonic environment[25,44] and comparable to those occurring in volcanic regions[9,45], where pronounced seasonal velocity variations[9] are similarly detected, and where the presence of large amount of preexisting microcracks can be a common condition.

To assess the depth at which seismic velocity variations occur, we computed the depth sensitivity of surface waves[46] for a local 1D velocity model[47]. The sensitivity of surface wave (see Methods) in the analyzed frequency band (0.5–1.0 Hz[25],) is concentrated in the first few kilometers of the crust (depth < 1.5 km, see Fig. S1), which include the thickness of highly-permeable, fractured carbonate rocks[41] forming the karst aquifer. However, the theoretical depth sensitivity of the scattered body waves, computed as in ref. 25 considering a 3D sensitivity kernel formulation[48] (see "Methods"), shows that the kernel is sensitive to a deeper volume in the crust than for surface waves (Fig. S1). The uncertainty in the nature of scattered waves challenges a precise attribution of the velocity variations observed at MCRV, which could be related to both the shallow highly-permeable, fractured carbonate rocks and the deeper seismogenic volume. Improving the reliability of sensitivity kernels is crucial to address and solve the depth resolution problem[49]. Additionally, independent information is provided by time-dependent P and S wave tomographic models, with poorer intensity and temporal sensitivity but higher spatial resolution. These analyses show significant temporal variations of Vp/Vs ratio below 6 km depth correlated with hydrological forcing[50] supporting the hypothesis of significant nonlinear effects at similar depths.

We estimated the strain variations (positive extensional strain) induced by the hydrological cycle (Fig. 2), by computing a 14 years-long time series of horizontal strain, that we modeled with a 3.5 km-thick layer of elementary cuboid sources[51] in the IFZ area (similar approach as in ref. 32, see "Methods"). To remove the long-term tectonic component and mitigate the temporal high-frequency noise and daily scatter, raw GPS time series have been initially detrended and low-pass filtered using a Gaussian filter (full-width 180 days). Two snapshots illustrating the regional NNE-SSW extension during wet periods and contraction in dry periods are reported in Fig. 2a, b, respectively, while the horizontal dilatational strain at MCRV is reported in Fig. 2c. The $\delta v/v$ follows the evolution of strain, with positive $\delta v/v$ for contractional strains and negative $\delta v/v$ associated with extension (Fig. 2c), consistent with previous natural[12,24,52] and laboratory experiments[2,21,27]. We remark that in the two episodes (Fig. 2a, b) the displacement at MCRV is oriented respectively NE (Fig. 2a) and SW (Fig. 2b), suggesting that the horizontal dilatation induced by hydrological forcing occurs along a single axis during both the recharge/discharge phases. Figure 2d represents the frequency of the compressional (left) and extensional (right) axis azimuth, coupled with the sign of the temporally coincident strain (top) and velocity variations (bottom) series. In particular, the frequency of the compressional (extensional) axis is counted when the dilatation is negative (positive). During summer, when strain is positive (red color), the extensional axis is oriented mostly W-NW, while during winter, when strain is negative (blue color), a similar orientation is shown by the compressive axis. The same happens when looking at velocity variations; during summer (winter) the velocity changes are negative (positive) and the extensional (compressional) axis is oriented mostly W-NW. We attribute the uniaxial strain fluctuation to an anisotropic poroelastic response[53] of the crust due to hydrological forcing[32] (hydraulic head Δh in karst aquifers). The horizontal strain ε_{xx} in the ENE-WSW direction (taken here as the x axis, see Supplementary Material for the complete derivation) can thus be expressed as:

$$\varepsilon_{xx} = \frac{\alpha \rho_w g \Delta h}{\frac{E\nu}{(1+\nu)(1-2\nu)}} \tag{3}$$

where α is the Biot's coefficient, ρ_w is water density, g is the gravity acceleration, E is the Young's modulus and ν is the Poisson's coefficient. We test the validity of our model considering a realistic water table variation $\Delta h = 20–40$ m[32] and a reasonable range of upper crust poroelastic parameters for carbonate rocks ($E = 60 - 80 GPa$, $\nu = 0.2 - 0.3$, $\alpha = 0.6 - 0.8$[54];). We estimate a strain variation in the order of $2 - 10 \times 10^{-6}$, whose lower bound is consistent with the range of observed non-tectonic strain variations within the decade-long time series (Fig.2c).

Non-linear elasticity

The observations summarized in Fig. 2, together with our simplified poroelastic model, suggest a strong coupling between $\delta v/v$ and strain

https://doi.org/10.1038/s41467-024-54094-4

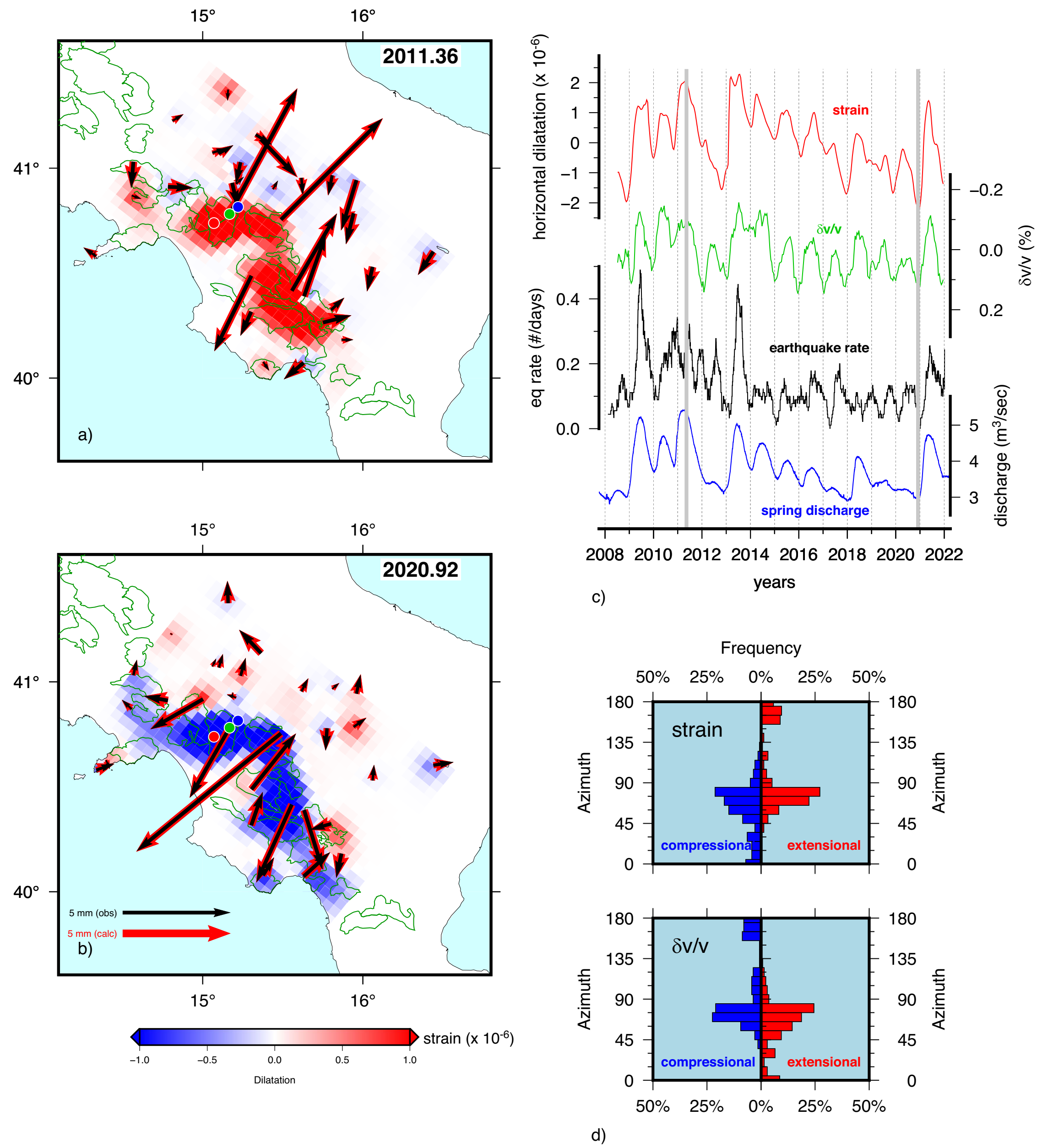

Fig. 2 | Deformation, Seismic velocity changes and hydrological forcing. **a**, **b** Maps of distributed hydrological strain with calculated/observed GPS displacements. The complete, continuous strain evolution is shown in Supplementary Movie 1. The two frames display opposite conditions of groundwater recharge in karst aquifers (shown as green lines) and opposite dilatational patterns. Red, green, and blue circles in (**a**) indicate data points where series of dilatational strain, velocity variations, and spring discharge (shown in (**c**)) have been respectively calculated. **c** Time series of dilatational strain (red) calculated at MCRV compared with the co-located velocity variations (green), earthquake rate (black), and Caposele spring discharge (blue); **d** frequency of the azimuth of compressional axis (*left*) and extensional axis (*right*) coupled with the sign of the synchronized scalar of the strain (*top panel*) and velocity changes (*bottom panel*).

in saturated crustal rocks. The oscillatory change in velocity with strain (Fig. 2) is similar to observations in laboratory-scale experiments[2,21], and can be exploited to study the nonlinear elastic response of crustal rocks following equation [2]. A comparison between $\delta v/v$ and strain values (Fig. 3a) shows a general inverse relationship ($\beta = -0.64 \times 10^{-3}$) indicating that, on average, seismic waves are slower when rocks are extended during maximum hydrological forcing (May-July), that when compressed during minimum hydrological forcing (December-January). This mechanism is consistent with the opening and closing of cracks and pores[6,13,52] with increasing stiffness of their internal contacts during compression[27].

The observed sensitivity β aligns with the values observed in previous works (-1×10^3–10^5)[12,13,24]. We also observe a complex, non-unique correspondence between velocity variations and strain, attributed to the superposition of seasonal and multiyear forcing cycles[31]. This superposition results in annual trajectories with similar slopes but different cycle means along the $\delta v/v$ axis (Fig. 3c–h). Additional information on the strain-rate dependency of seismic velocity variations can be inferred from the hysteretic behavior of $\delta v/v$ and strains[3,8]. For annual cycles defining closed or semi-closed loops (Fig. 3c–h), we observe prevalent clockwise loops but no evidence that seismic velocities are systematically higher during extension (Fig. 3b). We also do not observe a dependency of the cycles pattern upon strain magnitude.

It has been suggested[3] that the mechanism controlling quadratic nonlinearity (i.e., β) is distinct from the mechanisms

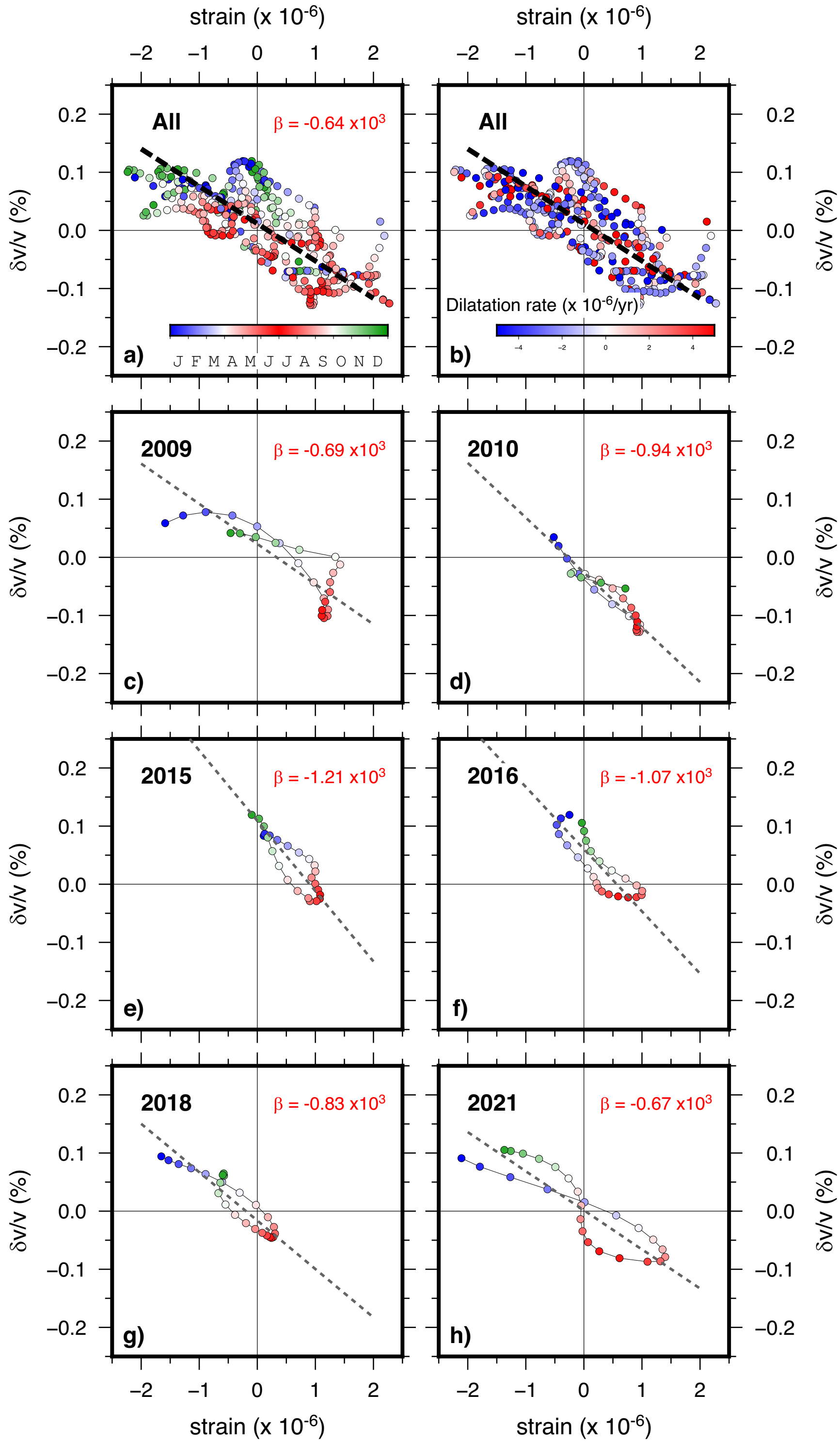

Fig. 3 | Strain sensitivity analysis of seismic velocity variations. **a** seismic velocity variations ($\delta v/v$) plotted against dilatational strain, color-coded for annual phase (capital letters in the colorbar indicate each month). The black dashed line shows the best-fit regression line whose slope (β) represents the strain sensitivity of velocity variations. **b** same as (**a**) but color-coded for dilatational rate. **c**–**h** specific annual cycles (year labeled on top left) color-coded for annual phase.

controlling additional nonlinear parameters (i.e., average softening and hysteresis). This distinction[3,26] may depend on the primary deformation mode across the interfaces (cracks or pores) within the bond system. Longitudinal deformation perpendicular to cracks or low-aspect ratio pores would control β, whereas shear deformation across the interfaces being responsible for average softening and hysteresis.

Possible factors arising from the calculation of strain that may affect the estimation of β are two folds. The first is the spacing of geodetic stations (tens of kilometers), larger than the dimension of the karst aquifer (Fig. 1), likely providing a lower boundary on the estimated strain. The second is the use of surface measurements of strain as representative of the actual values at depths (likely to be lower) where seismic velocity changes occur. These two factors, which cannot

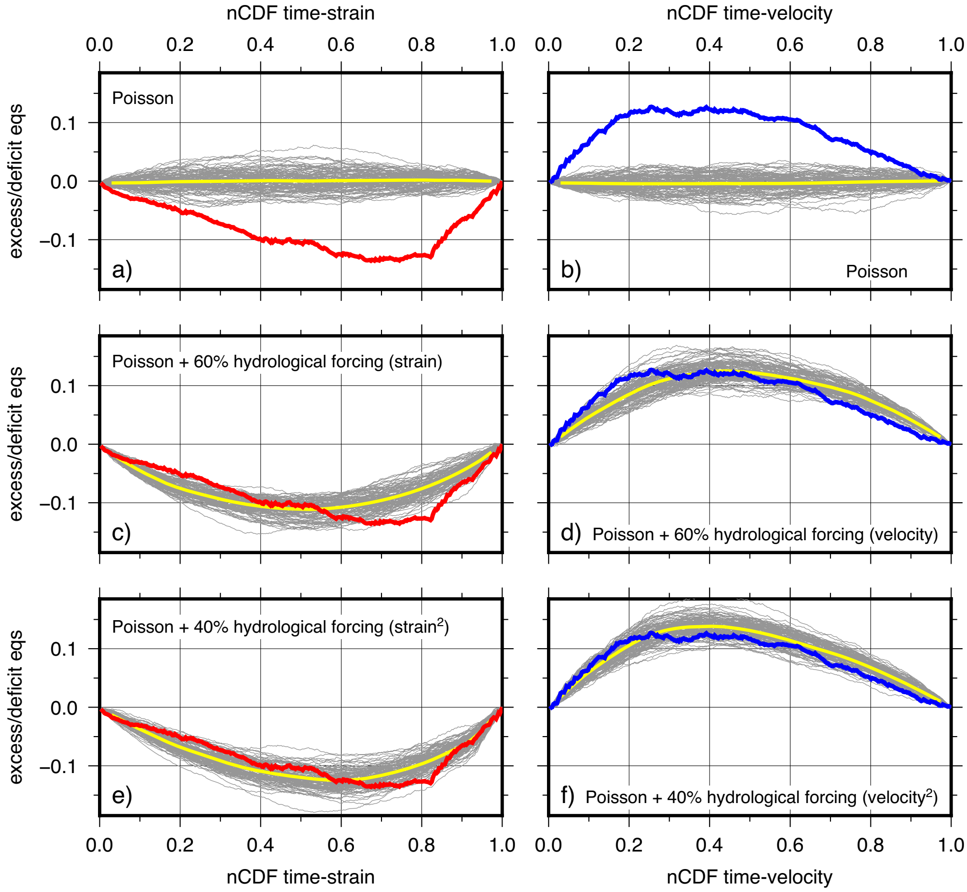

Fig. 4 | Modified quantile-quantile plots (QQP) to test correlation of seismicity rate with strain and seismic velocity variations. The vertical axis is a measure of excess or deficit of earthquakes at a given level of strain (in red, plots **a**, **c**, **e**) or velocity (in blue, plots **b**, **d**, **f**) based on the amount of time spent at or below that level. The horizontal axis is the normalized Cumulative Density Function (nCDF) of time-strain (or time-velocity). Gray lines show synthetic realizations (mean shown in yellow) with variable contribution and increasing effect of hydrological forcing.

be easily quantified, have opposite effects and will probably affect the value of β but not its sign.

Seismicity modulation

It has been previously reported that seismicity along the IFZ is modulated at seasonal and multiannual time scales by hydrological forcing from the karst aquifers[32]. The low values of estimated hydrologically-induced stress variations[32], corresponding to the observed seismicity modulation, suggest a critical state of stress for the faults within the actively deforming area, as observed in other actively-deforming regions where seismicity is triggered by small stress changes[55]. To investigate the relation between rock properties modulated by the hydrological forcing (strain and seismic velocity variations) and earthquake nucleation we declustered the seismic catalog along the IFZ (color-coded circles in Fig.1 c) and calculated the daily seismicity rates within 90-days moving windows (see Methods). This modulation is clearly displayed in the multiyear time series of Fig. 2c (where all the different observables have been resampled and synchronized at a 0.04-year step), showing in-phase peaks of seismicity rate, $\delta v/v$, strain and spring discharge. We also observe that the three largest peaks of seismicity rates in 2009, 2013 and 2021 (Fig. 2c), correspond to large seasonal increments in spring discharge (>2 m^3/s) and dilatational strain (>1×10^{-6}). We test the relationship between background seismicity and hydrological forcing (expressed as variations of dilatational strain or seismic velocity), following the approach of ref. 56 using a modified quantile-quantile plot (QQP). QQP tests for a specific relationship between hydrological forcing and seismicity rate rather than simply asking the question if earthquake occurrence is correlated with such forcing. In our case we plot the normalized cumulative fraction of earthquake rates that occurs at or below a given level of strain or seismic velocity against the normalized cumulative fraction of time that is spent at or below the same given level. To facilitate interpretation, we follow ref. 56 and modify the QQP plots to show excess or deficit of earthquakes by removing the 1:1 trend line. In the case of no correlation between the earthquake rate and hydrological forcing (either the strain or velocity variations), we expect to see a horizontal line because the fraction of earthquakes below a given level should be equivalent to the fraction of time spent at or below that level. If a point falls below the horizontal line, then there is a deficit of earthquakes up to the corresponding value compared with what is expected for time spent up to the corresponding value. If the point falls above, the opposite is true, which means we have an excess of earthquakes. We found (red lines in Fig. 4a) a deficit of earthquakes for low values of the strain compared to the case in which there would be no correlation with the strain (e.g., in the case of a Poisson process). This indicates that seismicity and hydrologically-related strains are correlated with each other. Moreover, the curve is slightly skewed to the right (Fig. 4a), showing that seismicity rate responds non-linearly to increasing strains explaining also the large response of seismicity to the largest strain increase in 2009, 2013 and 2021. As expected, the same analysis with velocity variations (Fig. 4b), shows an opposite behavior and an excess of earthquakes during low values of seismic velocity. Therefore, earthquakes occurrence and velocity variations are anti-correlated. In this second case, the curve is also skewed to the left (Fig. 4b), showing that seismicity rate also responds non-linearly to increasing velocity variations. The gray lines shown in Fig. 4a, b display 100 random permutations of the observed catalog which are cloudily disposed around the horizontal line showing that, when the catalog is randomized, no correlation is present with either strain (Fig. 4a) or seismic velocity variations (Fig. 4b). By comparing the observed seismicity rate with synthetic rate histories containing both random and hydrological components, we could estimate the level of hydrological forcing in the real catalog (see Methods). Figure 4(c–f) shows that the observed nCDFs of the observed seismicity require ~40% contribution of hydrological forcing and an increasing effect of strain or seismic velocity variation to reproduce the observed skewness, i.e., a non-linear influence of strain or seismic velocity variations on the seismicity rate.

Discussion

We measured hydrologically-modulated velocity changes $\delta v/v$ in the order of ~0.2% near the karst aquifers close to IFZ. Those variations are one order of magnitude smaller (~0.03%) at around 25 km distance, where the amplitudes of horizontal transient displacements are negligible too (Fig. 1c). Our primary observation shows that velocity is systematically slower during extension and higher during compressional strains resulting in a seasonally-controlled variation of the state of rock damage. Variations of elastic properties and their non-linear sensitivity to strain arise from the stiffness modification of the grain and fracture contacts. We thus propose that seasonal variations induce a weakening/healing process that cyclically affects the crust along the IFZ. The process we observe seems to be reversible, with a restoration of the initial conditions (and of the elastic properties), like a fault healing process[57] by which the crust retrieves its original characteristics prior to the new damage episode. Geodetic strain allows us to precisely track the mechanism underlying the velocity variations, which is the cyclical crack opening/closing of NW-SE-oriented crack system in the direction of the regional direction of minimum horizontal stress.

We observe that significant non-linear seasonal variations of elastic properties of the crust along the IFZ are statistically correlated with earthquakes rate. We propose a model in which hydrological deformations promote earthquake failure by a mechanism involving dynamic nonlinear elasticity[22]. Seasonal variations of elastic properties cause a weakening that triggers the observed micro-seismicity, alternated to a healing process as the strain amplitudes decrease and seismic wave velocity increases with frictional contacts ageing[20]. In terms of frictional contacts, we may also interpret triggering as the onset of sliding of the faults, resulting from an abrupt decrease in the shear strength of the fault gouge by softening of frictional contacts. Necessary physical characteristics for this triggering mechanism require a weak fault in a critical state and dynamic strain amplitudes greater than about 10^{-6}[18], regardless of their frequency content[58]. Both requirements are satisfied along the IFZ where active tectonic strain is likely to keep faults close to failure and hydrological forcing provides sufficient oscillatory strains. For the recent background micro seismicity, no significant localization along the segments responsible for the 1980 Ms 6.9 earthquake is observed[59] suggesting that a diffused triggering mechanism in the volume interested by hydrological forcing and resulting nonlinear reduction of elastic properties is more likely than an accelerated aseismic slip along major fault zones.

Laboratory experiments[22] show that modulus reduction increases progressively as the effective stress is reduced, implying that the system's elastic nonlinearity is strongly sensitive to increase in pore pressure. In agreement with the observed depth distribution of seismicity (Fig. S1), the deeper parts of the crust, where pore pressure may be greater than hydrostatic, may thus be more sensitive to hydrological forcing with respect to the shallow crust where extensive fracturing maintains a hydrostatic profile. The observed relationship between seismicity triggering and modulus reduction (Fig. 4e, f) also agrees with laboratory experiments[18] showing the existence of an approximate strain threshold above which significant elastic nonlinearity is observed and earthquakes are easily triggered. Thus, our study suggests that the elastic nonlinearity of fault cores close to a critical state plays a major role in earthquake triggering and offers an alternative perspective beyond models based solely on the evolution of pore pressure or Coulomb stress. We speculate that regional weakening of active fault zones, over time scales relevant for earthquake nucleation, may also increase the likelihood of higher-magnitude ruptures on large fault systems.

Methods

Velocity changes from Coda Wave Interferometry

We computed the three-component (ZZ, EE, NN) autocorrelation using continuous seismic data recorded at the MCRV station located in the IFZ area, in Southern Italy (Fig. 1a). The considered time window for this study is from January 2008 to December 2021. We rejected daily traces if they don't contain more than 20 h of data available and to reduce transient signals, we carried out a one-bit normalization.

We measured the velocity variations using the stretching technique[60], which provides stable measurements[25], by stacking 90 days using an 89-day overlap of correlations. The stack of the autocorrelation over the full-time period was used as the reference signal to compute relative velocity variations. This operation was performed for each component in the coda wave window starting at 10 s from the arrival of ballistic waves and with a duration of 40 s. The choice of this window allows to resolve changes of $\delta v/v$ in the shallow crust[25]. Velocity variations of the three components are, then, combined weighting with squared correlation coefficients estimated after stretching. We then select the velocity variations with correlation coefficients above 0.85.

In Fig. 1c we represent the comparison of the seismic velocity variation for the stations MCRV and CAFE, this latter being outside the carbonates and characterized by much smaller variations (around 34% compared to MCRV), demonstrating that the response of crust around MCRV is very peculiar and associated with the local characteristics of the complex IFZ.

Depth sensitivity kernels

We computed the depth sensitivity of surface waves (Fig. S1c, d) as in ref. 46 for a local velocity model[47] and for the frequency band 0.5–1.0 Hz at which we computed the velocity variations. This frequency band has been selected as it is the optimal band used in the Apennines to have a good temporal resolution with high quality correlation while limiting the number of stacked days[25,44,61]. For autocorrelations, the better outcomes are observed for frequencies exceeding 0.5 Hz[62], because in Southern Europe seasonal variations in the distribution of noise sources reduce the quality of the correlations and thus limit time dependent analysis[63], while frequencies higher than 1 Hz are too much contaminated by anthropogenic noise. We also computed the theoretical depth sensitivity of the scattered body waves (Fig. S1e) as in ref. 25, considering a 3D sensitivity kernel formulation[48]. We solved for the body wave depth sensitivity normalized to 30 km depth with each layer 1 km thick layer[25]. In our case we considered a coda time lapse 30 s, representative of the time window 10–50 s, and two free path (10,100 km) as reference.

Horizontal strain

Continuous surface displacements have been measured by permanent GPS stations of the RING network (http://ring.gm.ingv.it). For our analysis, we considered the time series of horizontal components corrected for the long-term tectonic trend and instrumental offset from January 2008 through December 2021 obtained following the procedure outlined in ref. 32. We calculate the time-dependent horizontal strain rate tensor at the surface by modeling the observed displacement with elementary cuboid sources extending to a depth of 3.5 km[51] following the approach described in ref. 32. The use of this modeling approach (fully described in ref. 51) to calculate the horizontal components of the "hydrological" strain rate field is required by the need to regularize the sparse density coverage of the GPS stations and incorporate the geometry of the karst aquifers. The second invariant of the horizontal long-term, tectonic strain rate field shown in Fig. 1a, has been obtained from the secular GPS velocity field of ref. 64 and using the VISR code[65] to calculate a regular grid of the horizontal strain rate tensor.

Seismicity and synthetic catalogs

IFZ is monitored since 2007 by the Irpinia Near Fault Observatory (*INFO*), which includes the Irpinia Seismic Network (*ISNet*, http://isnet.unina.it, network code IX), composed of a total of 31 co-located triaxial strong motion accelerometers and three-components short period or broad-band seismometers and 8 INGV seismic stations (https://eida.ingv.it/it/, virtual network _NFOIRPINA, network code IV). The period analyzed in the present study ranges from January 2008 through December 2021. The original data set consisted of 1898 events with local magnitude $-0.4 \le M_L \le 3.7$, and the seismicity is mostly concentrated at depths between 8 and 12 km (Fig. 1c, S1). To avoid biases associated to aftershocks, we declustered the earthquake catalog using the approach described in ref. 66, and its windowing technique, where a scan of the catalog within distance and time is performed with spatiotemporal windows as a function of the magnitude[66]. In this procedure, the first shock is not necessarily the largest shock in the sequence; thus, a small foreshock is the first event of an aftershock sequence. If a largest shock occurs in the series, this enlarges the window beyond the value used for the first shock[66]. Since the recorded seismicity may be affected by the detection capability of the network, we select events shallower than 12 km with magnitude above the minimum magnitude of completeness (M_C), i.e., the magnitude above which the network is assumed to reliably record all the events occurring in the region of interest, estimated at M_L 1.1 for *ISNet*[67]. Then we computed the seismicity rate as the number of earthquakes occurring in 90-days moving windows. We also tested the sensitivity of the seismicity rate to the parameters of the windowing technique[66] used for the declustering and we found that seismicity rate is not changed at all by varying the windows used (Fig. S2, Supplementary Materials). We constructed the synthetic catalogs starting from the observed number of events occurring in the considered time interval and considering this number as resulting from the sum of an homogeneous Poisson process and a nonhomogeneous hydrological forcing. The nonhomogeneous contribution has been produced using the inversion method[68] which involves firstly obtaining the cumulative distribution for the variable to be sampled (strain or seismic velocity). Cumulative distribution functions of the strain and seismic velocity variations (simple or squared to consider the case of linear and nonlinear effects, respectively) are calculated from the respective time series and rearranged to give an expression for the variable of interest (strain or seismic velocity) in terms of its probability. The variable can then be sampled by inserting uniform random values between 0 and 1 into this expression for each event contributing to the nonhomogeneous part of the synthetic catalog. The same approach has been used to calculate the homogeneous Poissonian contribution to the synthetic catalogs randomly sampling the cumulative function of the exponential distribution which controls the distribution of time intervals between successive independent events in a Poisson process[68]. Synthetic seismicity rate histories (90-days moving windows) are then computed from the synthetic catalogs.

Data availability

The seismic catalog can be downloaded at http://isnet.unina.it. Velocimetric continuous data are available at https://eida.ingv.it/it/. Raw GPS data (rinex files) are available at http://ring.gm.ingv.it. The time series of the discharge of Caposele spring has been provided by Approvviggionamento Idrico (DIRAP), Acquedotto Pugliese, S.p.a., Bari. The dataset of seismic velocity changes, geodetic strain, and seismicity rate, generated during the current study, is available from the corresponding author on reasonable request. Analysis was made using MATLAB (release 2023a, https://www.mathworks.com/products/matlab.html) and Python (https://www.python.org/). Correspondence and material requests should be addressed to S.T. at the following address: stefania.tarantino@ingv.it.

Code availability

This study was performed using the Python package Obspy and uses workflows provided in ref. 25 and ref. 32 for velocity variations measurement and strain computation respectively.

References

1. Zener, C. *Elasticity and Anelasticity of Metals* (The University of Chicago Press, 1948).
2. Renaud, G., Le Bas, P.-Y. & Johnson, P. A. Revealing highly complex elastic nonlinear (anelastic) behavior of Earth materials applying a new probe: dynamic acoustoelastic testing. *J. Geophys. Res. Solid Earth* **117**, n/a-n/a (2012).
3. Simpson, J., Malcolm, A. E. & van Wijk, K. The effect of temperature on the nonlinear elasticity of a fault rock in dynamic acoustoelastic testing (DAET) experiments. *Geophys. J. Int.* **235**, 554–565 (2023).
4. Lieou, C. K. C., Daub, E. G., Ecke, R. E. & Johnson, P. A. Slow dynamics and strength recovery in unconsolidated granular Earth materials: a mechanistic theory. *J. Geophys. Res. Solid Earth* **122**, 7573–7583 (2017).
5. Ostrovsky, L. A. & Johnson, P. A. Dynamic nonlinear elasticity in geomaterials. *La Riv. del. Nuovo Cim.* **24**, 1–46 (2001).
6. Renaud, G., Callé, S. & Defontaine, M. Remote dynamic acoustoelastic testing: elastic and dissipative acoustic nonlinearities measured under hydrostatic tension and compression. *Appl. Phys. Lett.* **94**, 011905 (2009).
7. Jin, J., Rivière, J., Ohara, Y. & Shokouhi, P. Dynamic acousto-elastic response of single fatigue cracks with different microstructural features: an experimental investigation. *J. Appl. Phys.* **124**, 075303 (2018).
8. Delorey, A. A., Guyer, R. A., Bokelmann, G. H. R. & Johnson, P. A. Probing the damage zone at parkfield. *Geophys. Res. Lett.* **48**, e2021GL093518 (2021).
9. Wang, Q.-Y. et al. Seasonal crustal seismic velocity changes throughout Japan. *J. Geophys. Res. Solid Earth* **122**, 7987–8002 (2017).
10. Clements, T. & Denolle, M. A. Tracking groundwater levels using the ambient seismic field. *Geophys. Res. Lett.* **45**, 6459–6465 (2018).
11. Mao, S., Lecointre, A., van der Hilst, R. D. & Campillo, M. Space-time monitoring of groundwater fluctuations with passive seismic interferometry. *Nat. Commun.* **13**, 4643 (2022).
12. Takano, T., Nishimura, T., Nakahara, H., Ohta, Y. & Tanaka, S. Seismic velocity changes caused by the Earth tide: ambient noise correlation analyses of small-array data. *Geophys. Res. Lett.* **41**, 6131–6136 (2014).
13. Takano, T., Nishimura, T., Nakahara, H., Ueda, H. & Fujita, E. Sensitivity of seismic velocity changes to the tidal strain at different lapse times: data analyses of a small seismic array at Izu-Oshima Volcano. *J. Geophys. Res. Solid Earth* **124**, 3011–3023 (2019).
14. Delorey, A. A., van der Elst, N. J. & Johnson, P. A. Tidal triggering of earthquakes suggests poroelastic behavior on the San Andreas Fault. *Earth Planet Sci. Lett.* **460**, 164–170 (2017).
15. Delorey, A. A., Bokelmann, G. H. R., Johnson, C. W. & Johnson, P. A. Estimation of the orientation of stress in the Earth's crust without

earthquake or borehole data. *Commun. Earth Environ.* **2**, 190 (2021).
16. Ben-Zion, Y. Collective behavior of earthquakes and faults: continuum-discrete transitions, progressive evolutionary changes, and different dynamic regimes. *Rev. Geophys.* **46**, RG4006 (2008).
17. Ben-Zion, Y. & Zaliapin, I. Spatial variations of rock damage production by earthquakes in southern California. *Earth Planet Sci. Lett.* **512**, 184–193 (2019).
18. Johnson, P. A. & Jia, X. Nonlinear dynamics, granular media and dynamic earthquake triggering. *Nature* **437**, 871–874 (2005).
19. Niu, F., Silver, P. G., Daley, T. M., Cheng, X. & Majer, E. L. Preseismic velocity changes observed from active source monitoring at the Parkfield SAFOD drill site. *Nature* **454**, 204–208 (2008).
20. Scuderi, M. M., Marone, C., Tinti, E., Di Stefano, G. & Collettini, C. Precursory changes in seismic velocity for the spectrum of earthquake failure modes. *Nat. Geosci.* **9**, 695–700 (2016).
21. Rivière, J. et al. Frequency, pressure, and strain dependence of nonlinear elasticity in Berea Sandstone. *Geophys Res Lett.* **43**, 3226–3236 (2016).
22. Tinti, E. et al. On the evolution of elastic properties during laboratory stick-slip experiments spanning the transition from slow slip to dynamic rupture. *J. Geophys. Res. Solid Earth* **121**, 8569–8594 (2016).
23. Shapiro, N. M. & Campillo, M. Emergence of broadband Rayleigh waves from correlations of the ambient seismic noise. *Geophys. Res. Lett.* **31**, n/a-n/a (2004).
24. Hillers, G. et al. In situ observations of velocity changes in response to tidal deformation from analysis of the high-frequency ambient wavefield. *J. Geophys. Res. Solid Earth* **120**, 210–225 (2015).
25. Poli, P., Marguin, V., Wang, Q., D'Agostino, N. & Johnson, P. Seasonal and coseismic velocity variation in the region of L'Aquila from single station measurements and implications for crustal rheology. *J. Geophys. Res. Solid Earth* **125**, e2019JB019316 (2020).
26. Sens-Schönfelder, C., Snieder, R. & Li, X. A model for nonlinear elasticity in rocks based on friction of internal interfaces and contact aging. *Geophys. J. Int.* https://doi.org/10.1093/gji/ggy414 (2018).
27. Grêt, A., Snieder, R. & Scales, J. Time-lapse monitoring of rock properties with coda wave interferometry. *J. Geophys. Res. Solid Earth* **111**, n/a-n/a (2006).
28. Bernard, P. & Zollo, A. The Irpinia (Italy) 1980 earthquake: detailed analysis of a complex normal faulting. *J. Geophys. Res.* **94**, 1631 (1989).
29. Leone, G. et al. A hundred years of Caposele spring discharge measurements: trends and statistics for understanding water resource availability under climate change. *Stoch. Environ. Res. Risk Assess.* **35**, 345–370 (2021).
30. Fiorillo, F. Spring hydrographs as indicators of droughts in a karst environment.*J. Hydrol.* **373**, 290–301 (2009).
31. Silverii, F., D'Agostino, N., Métois, M., Fiorillo, F. & Ventafridda, G. Transient deformation of karst aquifers due to seasonal and multiyear groundwater variations observed by GPS in southern Apennines (Italy). *J. Geophys. Res. Solid Earth* **121**, 8315–8337 (2016).
32. D'Agostino, N. et al. Crustal deformation and seismicity modulated by groundwater recharge of karst aquifers. *Geophys. Res. Lett.* **45**, 12,253–12,262 (2018).
33. Heki, K. Snow load and seasonal variation of earthquake occurrence in Japan. *Earth Planet Sci. Lett.* **207**, 159–164 (2003).
34. Saar, M. O. & Manga, M. Seismicity induced by seasonal groundwater recharge at Mt. Hood, Oregon. *Earth Planet. Sci. Lett.* **214**, 605–618 (2003).
35. Bettinelli, P. et al. Seasonal variations of seismicity and geodetic strain in the Himalaya induced by surface hydrology. *Earth Planet Sci. Lett.* **266**, 332–344 (2008).
36. Craig, T. J., Chanard, K. & Calais, E. Hydrologically-driven crustal stresses and seismicity in the New Madrid Seismic Zone. *Nat. Commun.* **8**, 2143 (2017).
37. Johnson, C. W., Fu, Y. & Bürgmann, R. Seasonal water storage, stress modulation, and California seismicity. *Science* **356**, 1161–1164 (2017).
38. Handwerger, A. L., Huang, M.-H., Fielding, E. J., Booth, A. M. & Bürgmann, R. A shift from drought to extreme rainfall drives a stable landslide to catastrophic failure. *Sci. Rep.* **9**, 1569 (2019).
39. Hsu, Y.-J. et al. Synchronized and asynchronous modulation of seismicity by hydrological loading: a case study in Taiwan. *Sci. Adv.* **7**, eabf7282 (2021).
40. Xue, L., Johnson, C. W., Fu, Y. & Bürgmann, R. Seasonal seismicity in the western branch of the East African Rift system. *Geophys. Res. Lett.* **47**, e2019GL085882 (2020).
41. Ascione, A., Mazzoli, S., Petrosino, P. & Valente, E. A decoupled kinematic model for active normal faults: Insights from the 1980, MS = 6.9 Irpinia earthquake, southern Italy. *Geol. Soc. Am. Bull.* **125**, 1239–1259 (2013).
42. De Matteis, R. et al. Fault Delineation and regional stress direction from the analysis of background microseismicity in the Southern Apennines, Italy. *Bull. Seismol. Soc. Am.* **102**, 1899–1907 (2012).
43. D'Agostino, N. Complete seismic release of tectonic strain and earthquake recurrence in the Apennines (Italy). *Geophys. Res. Lett.* **41**, 1155–1162 (2014).
44. Barajas, A., Poli, P., D'Agostino, N., Margerin, L. & Campillo, M. Separation of poroelastic and elastic processes of an aquifer from tectonic phenomena using geodetic, seismic, and meteorological data in the Pollino region, Italy. *Geochem. Geophys. Geosyst.* **22**, e2021GC009742 (2021).
45. Brenguier, F. et al. Mapping pressurized volcanic fluids from induced crustal seismic velocity drops. *Science (1979)* **345**, 80–82 (2014).
46. Herrmann, R. B. Computer programs in seismology: an evolving tool for instruction and research. *Seismol. Res. Lett.* **84**, 1081–1088 (2013).
47. Matrullo, E., De Matteis, R., Satriano, C., Amoroso, O. & Zollo, A. An improved 1-D seismic velocity model for seismological studies in the Campania–Lucania region (Southern Italy). *Geophys J. Int* **195**, 460–473 (2013).
48. Pacheco, C. & Snieder, R. Time-lapse travel time change of multiply scattered acoustic waves. *J. Acoust. Soc. Am.* **118**, 1300–1310 (2005).
49. Barajas, A., Margerin, L. & Campillo, M. Coupled body and surface wave sensitivity kernels for coda-wave interferometry in a three-dimensional scalar scattering medium. *Geophys. J. Int.* **230**, 1013–1029 (2022).
50. De Landro, G. et al. Decade-long monitoring of seismic velocity changes at the Irpinia fault system (southern Italy) reveals pore pressure pulsations. *Sci. Rep.* **12**, 1–9 (2022).
51. Barbot, S., Moore, J. D. P. & Lambert, V. Displacement and stress associated with distributed anelastic deformation in a half-space. *Bull. Seismol. Soc. Am.* **107**, 821–855 (2017).
52. Yamamura, K. et al. Long-term observation of in situ seismic velocity and attenuation. *J. Geophys. Res. Solid Earth* **108**, 2317 (2003).
53. Segall, P. & Lu, S. Injection-induced seismicity: Poroelastic and earthquake nucleation effects. *J. Geophys. Res. Solid Earth* **120**, 5082–5103 (2015).
54. Mavko, G., Kjartansson, E. & Winkler, K. Seismic wave attenuation in rocks. *Rev. Geophys.* **17**, 1155 (1979).
55. Scholz, C. H. *The Mechanics of Earthquakes and Faulting*. (Cambridge University Press, 2019). https://doi.org/10.1017/9781316681473.
56. Delorey, A. A. & Chen, T. Behavior of tidally triggered earthquakes depends on fluid conditions. *Bull. Seismol. Soc. Am.* **112**, 2890–2901 (2022).

57. Brenguier, F. et al. Postseismic relaxation along the San Andreas fault at Parkfield from continuous seismological observations. *Science* **321**, 1478–1481 (2008).
58. Gomberg, J. & Johnson, P. Dynamic triggering of earthquakes. *Nature* **437**, 830–830 (2005).
59. De Landro, G. et al. High-precision differential earthquake location in 3-D models: evidence for a rheological barrier controlling the microseismicity at the Irpinia fault zone in southern Apennines. *Geophys. J. Int.* **203**, 1821–1831 (2015).
60. Lobkis, O. I. & Weaver, R. L. Coda-wave interferometry in finite solids: recovery of *P*-to-*S* conversion rates in an Elastodynamic Billiard. *Phys. Rev. Lett.* **90**, 254302 (2003).
61. Mikhael, N., Poli, P. & Garambois, S. Non-linear seismic velocity variations observed during a seismic swarm in the Alto Tiberina low angle normal fault from ambient noise correlation measurements. *J. Geophys. Res. Solid Earth* **129**, e2023JB028232. (2024).
62. Hobiger, M., Wegler, U., Shiomi, K. & Nakahara, H. Single-station cross-correlation analysis of ambient seismic noise: application to stations in the surroundings of the 2008 Iwate-Miyagi Nairiku earthquake. *Geophys J. Int* **198**, 90–109 (2014).
63. Stehly, L., Delouche, E., Tomasetto, L. & Ranjan, P. Dynamic of seismic noise sources in the Mediterranean Sea: implication for monitoring using noise correlations. *Comptes Rendus Géosci*. **356**, 1–24 (2024).
64. Daout, S. et al. Along-strike variations of strain partitioning within the Apennines determined from large-scale multi-temporal InSAR analysis. *Tectonophysics* **867**, 230076 (2023).
65. Shen, Z., Wang, M., Zeng, Y. & Wang, F. Optimal interpolation of spatially discretized geodetic data. *Bull. Seismol. Soc. Am.* **105**, 2117–2127 (2015).
66. Gardner, J. K. & Knopoff, L. Is the sequence of earthquakes in Southern California, with aftershocks removed, Poissonian? *Bull. Seismol. Soc. Am.* **64**, 1363–1367 (1974).
67. Vassallo, M., Festa, G. & Bobbio, A. Seismic ambient noise analysis in Southern Italy. *Bull. Seismol. Soc. Am.* **102**, 574–586 (2012).
68. Zhuang, J. & Touati, S. Stochastic simulation of earthquake catalogs, community online resource for statistical seismicity analysis. http://www.corssa.org (2015).
69. Wessel, P. et al. The generic mapping tools version 6. *Geochem. Geophys. Geosyst.* **20**, 5556–5564 (2019).
70. Galli, P. & Peronace, E. New paleoseismic data from the Irpinia Fault. A different seismogenic perspective for southern Apennines (Italy). *Earth Sci. Rev.* **136**, 175–201 (2014).

Acknowledgements

This work has been supported by the INGV-Pianeta Dinamico Project MYBURP (Modulation of hydrology on stress buildup on the Irpinia Fault) and the PRIN-FLUIDS project: "Detection and tracking of crustal fluid by multi-parametric methodologies and technologies" of the Italian PRIN-MIUR programme (Grant no. 20174X3P29). P.P. has been supported by the European Research Council (ERC) under the European Union Horizon 2020 Research and Innovation Program (grant agreements 802777—MONIFAULTS). Figures were generated with Generic Mapping Tools[69].

Author contributions

S.T., P.P., and N.D. conceived the methodology and wrote the first draft of the manuscript. S.T., P.P., N.D., G.F., and M.V. contributed to data preparation and analysis and to the interpretation of results. G.V. provided data of the Caposele spring. A.Z. contributed to the interpretation of results. All authors revised the final draft of the manuscript.

Competing interests

The authors declare no competing interests.

Additional information

Supplementary information The online version contains supplementary material available at https://doi.org/10.1038/s41467-024-54094-4.

Correspondence and requests for materials should be addressed to Stefania Tarantino.

Peer review information *Nature Communications* thanks Andrew Delorey and the other, anonymous, reviewer(s) for their contribution to the peer review of this work. A peer review file is available.